

# A practical approach to Hohenberg-Kohn maps based on many-body correlations: learning the electronic density

Edgar Josué Landinez Borda and Amit Samanta\*

*Physics Division, Lawrence Livermore National Laboratory, Livermore, California 94550, USA*

(Dated: June 6, 2022)

High throughput screening of materials for technologically relevant areas, like identification of better catalysts, electronic materials, ceramics for high temperature applications and drug discovery, is an emerging topic of research. To facilitate this, density functional theory based (DFT) calculations are routinely used to calculate the electronic structure of a wide variety of materials. However, DFT calculations are expensive and the computing cost scales as the cube of the number of electrons present in the system. Thus, it is desirable to generate surrogate models that can mitigate these issues. To this end, we present a two step procedure to predict total energies of large three-dimensional systems (with periodic boundary conditions) with chemical accuracy (1 kcal/mol) using a small data set, meaning that such models can be trained on-the-fly. Our procedure is based on the idea of the Hohenberg-Kohn map proposed by Brockherde et al. (Nat. Commun, **8**, 872 (2017)) and involves two training models: one, to predict the ground state charge density,  $\rho(\mathbf{r})$ , directly from the atomic structure, and another to predict the total energy from  $\rho(\mathbf{r})$ . To predict  $\rho(\mathbf{r})$ , we use many-body correlation descriptors to accurately describe the neighborhood of a grid point and to predict the total energy we use amplitudes of these many-body correlation descriptors. Utilizing the amplitudes of the many-body descriptors allows for uniquely identifying a structure while accounting for constraints, such as translational invariance; additionally, such a formulation is independent of the charge density grid.

## I. INTRODUCTION

Kohn-Sham density functional theory (DFT) is a popular technique that is commonly used to calculate the electronic structure of a wide variety of materials to predict, and/or to analyze their mechanical, optical, electronic, or magnetic properties. This success can be attributed to the fact that many physical and chemical properties of interest can be derived from the ground state electronic density,  $\rho(\mathbf{r})$ . Here,  $\rho(\mathbf{r})$  is a scalar field and  $\mathbf{r}$  corresponds to a point in the supercell. Typically, DFT calculations are limited to supercells containing a few hundred atoms, and due to the high computation cost associated with solving the eigenvalue problem of the Kohn-Sham Hamiltonian, typical systems in ab initio molecular dynamics (MD) simulations can be evolved only for a few tens of pico-seconds. This is orders of magnitude smaller than time-scales associated with physical processes such as phase transitions, conformational changes in molecules, or creep failure of a material. Thus, it is desirable to develop surrogate models that can speed up individual DFT calculations. Recently, a new set of methods based on machine learning approaches has been proposed that can overcome or bypass the bottleneck of traditional methods, and successfully predict molecular properties at lower computational cost.<sup>1</sup> These techniques explore the physical information of the data using statistical inference to train a model for the desired properties. The goal here is not to develop models that try to learn the Born-Oppenheimer potential energy surface for the whole configuration space, but to develop models that can learn only a part of the energy surface on-the-fly and speed up MD or Monte Carlo simulations. For example, Brockherde et al, in 2017 studied three different trained models:<sup>2</sup> (i) the orbital-free map, (ii) the Hohenberg-Kohn map, and (iii) the Kohn-Sham map. The orbital-free map method uses machine learning to predict the kinetic energy functional for a given ground state electronic density  $\rho(\mathbf{r})$ , and uses its functional derivative to self-consistently

solve the Euler equation. On the other hand, the Kohn-Sham map attempts to model the total energy as a functional of the external potential  $v(\mathbf{r})$ , and the Hohenberg-Kohn map is a two step procedure that first attempts to learn  $\rho(\mathbf{r})$  from  $v(\mathbf{r})$  and then predict the total energy from  $\rho(\mathbf{r})$ . In their formulation,  $v(\mathbf{r})$  is obtained from the superposition of Gaussian functions placed at the atomic positions and  $\rho(\mathbf{r})$  is represented using Fourier basis functions. These methods can be used to model total energies and charge density of small molecules like water, benzene and ethane. But, the fact that hundreds of structures are required to train models for systems containing only a few atoms poses a serious practical problem in using these for large systems (for example, crystalline solids, liquids). Thus, there is a need to develop models that can be trained using a much smaller data set.

The Hohenberg-Kohn map has many advantages: it is computationally more efficient than a direct DFT calculation and it is easy to parallelize on large computers. In addition, representing the nuclear potential using a set of Gaussians (weighted by their corresponding atomic numbers) allows trained models to easily handle multicomponent systems without increasing the computation cost. On the other hand, in many methods that have been proposed to predict  $\rho(\mathbf{r})$  directly from a set of atomic positions, the number of features/descriptors increases exponentially with the number of different elements present in the system. Such a problem can perhaps be circumvented by the method proposed by Ji and Jung in Ref [3]. These authors proposed a local environment descriptor based on the conjecture that information about the local environment surrounding a grid point can be compressed by spherical averaging. Therefore, the authors generated feature vectors for each grid point by averaging of pseudo-potentials over spheres of a pre-defined set of radii. Motivated by these results it is intuitive to ask if this feature vector can be used to directly predict the total energy from an external potential generated by a superposition of Gaus-

sians (proposed by Brockherde et al.)<sup>2</sup> or a superposition of pseudo-potentials (proposed by Ji and Jung)<sup>3</sup>.

Alternatively, Brockherde et al. proposed using a set of basis functions to represent  $\rho(\mathbf{r})$  in order to decrease the computational cost.<sup>2</sup> Here we note that in addition to the computational cost issue, for three-dimensional systems, such as crystalline solids or liquids, simple constraints like global translation and rotation, are difficult to implement in a grid-based representation framework. Thus, many researchers have also modeled the electronic charge density using a set of basis functions. For example, Grisafi et al. modeled the charge density using an atom-centered, symmetry-adapted Gaussian process regression framework.<sup>4,5</sup> Fabrizio et al. in Ref [6] used a similar approach to predict the ground state electronic charge density of a large number of dimers by using specialized basis sets, such as Weigend’s JK-fit cc-pVQZ.

Many researchers have also used neural networks to generate surrogate models. For example, Nagai et al.<sup>7</sup> modeled the electronic density and total energy with a flexible feed-forward neural network in which the exchange-correlation potential is obtained by taking functional derivatives using the back-propagation method. To make the model independent of the grid, the authors used quantities such as the local electronic density, local spin density and the scaled gradient of the electronic density. Similarly, Chandrasekaran et al. used a variety of scalar, vector and tensor fingerprints to train a neural network model.<sup>8</sup> On the other hand, in the PROPhet package developed by Kobl et al., the electronic charge density is predicted from the atomic position by training a neural network model that uses descriptors proposed by Behler and Parrinello.<sup>9</sup>

Sinitkiy and Pande, in contrast, proposed a deep neural network based scheme to capture subtle features of the electronic charge density, such as lone pairs and hybridized electronic shapes around aromatic and cyclopropane rings, with high accuracy.<sup>10</sup> Similarly, Dick and Fernandez-Serra have proposed a scheme to correct baseline DFT energies and forces to the accuracy provided by a higher level method.<sup>11</sup> From the computational point of view, such methods are very promising because the time required for charge density and total energy predictions are at least an order of magnitude lower than brute force DFT calculations. The advantages of such an approach, however, motivate the development of a similar framework for three-dimensional systems (with periodic boundary conditions) that satisfies global rotation and translation constraints. In addition, the necessity of a large training data set even in the cases where the preceding method is computationally viable serves as an additional motivating factor for the development of a method which is equally effective with less data.

Eric Schmidt and co-workers in Ref [12] modeled the ground state electronic density using a linear model that specifically included two- and three-body correlations:

$$\rho_e(\mathbf{r}) = \sum_{i=1}^N f_2(|\mathbf{r} - \mathbf{r}_i|) + \sum_{i,j=1}^N f_3(|\mathbf{r} - \mathbf{r}_i, \mathbf{r} - \mathbf{r}_j|). \quad (1)$$

Here  $N$  is the total number of atoms,  $i$  and  $j$  are indices of

atoms located at  $\mathbf{r}_i$  and  $\mathbf{r}_j$ , respectively, and  $f_2$  and  $f_3$  are functions of one and two variables that capture two- and three-body correlations. In Ref [12], it is reported that including the three-body contributions dramatically improves the predictive capability of the model as compared to a model containing only the two-body term. Next, the total energy is calculated from a sum of two contributions: (a) an embedding energy term that uses only the two-body contributions to the charge density in Eq. 1, and (b) a pair energy term that depends on the distance between an atom and its neighbors. Since this model was tested on a wide variety of systems (including metals, alloys, semi-metal, ceramic oxides), it is natural to ask if it is possible to develop a generalized representation of the electronic density that includes two-, three-, four-body and higher order correlation. Similarly, it is interesting to explore if the model to predict the total energy can also be systematically improved by including three-body and higher order correlations. If this is possible, then one can switch on or off terms based on the accuracy and computational cost trade-offs.

Here, we propose a general framework to learn a model of the ground state charge density using a many-body expansion. We show that the predictive capability can be enhanced by systematically incorporating two-, three-, four-body or higher order correlations. The total energy calculations, on the other hand, relies on a simple model that uses amplitudes of the many body contributions (to the charge density) as descriptors. These two models illustrate that these off-the-grid descriptors are enough to infer the energy landscape at a relatively small cost. In addition, a majority of the studies reported in the literature have focused on isolated systems. In contrast, we focus on full three dimensional periodic systems and explore avenues to predict  $\rho(\mathbf{r})$  and the total energy using different nonlinear regression and dimension reduction techniques.

The remainder of the paper takes the following form. In Section II, we present details of our models. In Section III, we use these models to predict ground state charge densities and total energies of amorphous structures of germanium. To this end, we analyze the importance of higher order correlations in accurately predicting the ground state charge density and compare models obtained from a variety of linear and nonlinear regression techniques.

## II. MODELS TO PREDICT THE ELECTRONIC CHARGE DENSITY AND THE TOTAL ENERGY

In the following discussion, in line with the Hohenberg-Kohn map framework, we present two methods: one to predict the ground-state electronic charge density from the atomic structure, and another to predict the total energy from the ground state electronic charge density. To predict  $\rho(\mathbf{r})$ , we propose an off-the-grid technique that relies on a set of descriptors that can effectively capture the local environment around an atom. As we show below, descriptors based on the two-, three-, four-body correlations can effectively capture the underlying symmetry of the distribution of atoms. These descriptors are then used to train a linear regression

based model using a set of training structures and their corresponding ground state charge densities.

To predict the total energy from the electronic charge density, the ground state electronic density of a given structure is first mapped to a unique point in the feature space. This representation is important to make the total energy predictions invariant to global rotation/translation of  $\rho(\mathbf{r})$  (and atomic positions) and to the ordering of grid indices. Next, we use a variety of linear and nonlinear regression techniques to predict the total energy from these features.

### A. Local correlation descriptors to predict the electronic density

In this section, we propose a set of descriptors that can be used to predict the ground state electronic charge density with high accuracy for three dimensional systems using as few structures, and corresponding charge densities, as possible for training. Since, a few methods have already been proposed with this objective, we want to develop a scheme that can allow us to systematically improve the accuracy, not simply by increasing the number of basis functions used as descriptors, but by adding higher order correlations thereby allowing us to control the trade-off between accuracy and computation cost. To design descriptors that embed local correlations,<sup>4,5,13-28</sup> we first consider how the effective electronic density of an atom is affected by the presence of other atoms. To this end, let us consider a structure  $S_u$  ( $u$  is the structure identification index) at a point  $\mathbf{X} \in \mathbf{R}^{3N}$  in the configuration space containing  $N$  atoms, located at  $\{\mathbf{r}_1, \mathbf{r}_2, \mathbf{r}_3, \dots, \mathbf{r}_N\}$ , such that  $\mathbf{r}_i \in \mathbf{R}^3$  for  $i = 1, 2, \dots, N$ . In addition, we assume the electronic density of an atom, with index  $i$ , when it is isolated from any other atoms, is represented by a smooth and differentiable function  $\rho_1(\mathbf{r}, \mathbf{r}_i)$ . We represent the effective electronic density of this atom, when placed amongst a distribution of other atoms (placed at  $\mathbf{r}_1, \mathbf{r}_2, \dots, \mathbf{r}_{N_i}$ ), by

$$\bar{\rho}(\mathbf{r}, \mathbf{r}_i | \mathbf{r}_1, \mathbf{r}_2, \dots, \mathbf{r}_{N_i}) = p_1 - p_2 + p_3 - p_4 + \dots \quad (2)$$

Here,  $p_1 = \rho_1(\mathbf{r}, \mathbf{r}_i)$ ,  $N_i$  is the number of neighbors of  $i$  and  $p_k$  is the overlap between the densities of the atom at  $\mathbf{r}_i$  and its  $k$  neighbors. Hence,  $p_k$  depends on the positions of neighbors of atom  $i$  meaning that  $\bar{\rho}(\mathbf{r}, \mathbf{r}_i | \mathbf{r}_1, \mathbf{r}_2, \dots, \mathbf{r}_{N_i})$  can capture many-body effects. For example, two-body correlations can be captured by the overlap between electronic densities of atom  $i$  and its neighbors

$$p_2(\mathbf{r}, \mathbf{r}_i | \mathbf{r}_1, \mathbf{r}_2, \dots, \mathbf{r}_{N_i}) = \sum_j \rho_1(\mathbf{r}, \mathbf{r}_i) \rho_1(\mathbf{r}, \mathbf{r}_j). \quad (3)$$

Here, the sum is over all possible neighbors of atom  $i$  in the system. Similarly, the overlap between the electronic densities of atom  $i$  and two of its neighbors (with indices  $j$  and  $k$ ) is

given by (see Fig. 1)

$$p_3(\mathbf{r}, \mathbf{r}_i | \mathbf{r}_1, \mathbf{r}_2, \dots, \mathbf{r}_{N_i}) = \sum_{j,k} \rho_1(\mathbf{r}, \mathbf{r}_i) \rho_1(\mathbf{r}, \mathbf{r}_j) \rho_1(\mathbf{r}, \mathbf{r}_k). \quad (4)$$

Following the same procedure as mentioned above, we can design descriptors to capture higher order correlations. For example, the overlap between electronic densities of atom  $i$  and three of its neighbors is given by

$$p_4(\mathbf{r}, \mathbf{r}_i | \mathbf{r}_1, \mathbf{r}_2, \dots, \mathbf{r}_{N_i}) = \sum_{j,k,l} \rho_1(\mathbf{r}, \mathbf{r}_i) \rho_1(\mathbf{r}, \mathbf{r}_j) \rho_1(\mathbf{r}, \mathbf{r}_k) \rho_1(\mathbf{r}, \mathbf{r}_l). \quad (5)$$

Here  $j, k$  and  $l$  are indices of three atoms in the neighborhood of atom  $i$ . Thus, if  $\rho(\mathbf{r}, \mathbf{r}_i)$  is known, the spatial variation in the effective density in Eq. 2 can be calculated by including the different correlations. Here we note that Eqs. 3-5 describe the correlation between atoms, and  $\mathbf{r}$  can be the spatial location of a grid point. Thus, in the following sub-sections, we use this notion to propose descriptors that can very effectively capture the local neighborhood information around a grid point.

#### 1. Two-body correlations

For a systematic analysis of correlations, the functional form of the electronic density  $\rho_1(\mathbf{r}, \mathbf{r}_j)$  of an isolated atom (located at  $\mathbf{r}_j$ ) is required. This quantity can be calculated using any first principles methodology, but to keep the formulation general, we use a set of orthogonal basis functions to capture these correlation descriptors.

To calculate two-body correlations, we need to capture the effect of the electronic density of an atom (located at  $\mathbf{r}_j$ ) on the grid point (located at  $\mathbf{r}$ ). Thus, we define

$$\sum_j \rho_1(\mathbf{r}, \mathbf{r}_j) = \sum_n c_n^{(21)} \phi_n^{(21)}, \quad (6)$$

where,  $\phi_n^{(21)} = \sum_j \psi_n(|\mathbf{r} - \mathbf{r}_j|)$ .

Here,  $\psi_n$  ( $n = 1, 2, 3, \dots$ ) is a set of orthogonal basis functions,  $\mathbf{r}$  is the spatial location of the grid point, the atom with index  $j$  is in the neighborhood of this grid point, and  $c_n^{(21)}$  are the coefficients of this expansion. It is worth noting that this two-body correlation captures the proximity between a grid point and an atom. Hence, it is different from the two-body correlation between two atoms that is defined in Eq. 3

#### 2. Nomenclature

To describe the different types of many-body correlations we use the following nomenclature. The number  $p$  in  $c^{(pq)}$  is the total number of atoms and grid points present in the corre-

lation and  $q$  denotes the number of bonds. For example, in a two-body correlation, an atom and a grid point are connected by a single bond. Thus,  $q = 1$  and  $p = 2$ . Similarly,  $c^{(33)}$  and  $c^{(32)}$  correspond to three-body correlations with three and two bonds, respectively (see Fig. 1). The number of bonds (i.e.  $q$ ) present in a correlation determines the number of orthogonal basis functions being multiplied and the computation cost increases exponentially as both  $p$  and  $q$  increases.

### 3. Three-body correlations

Next, we consider descriptors based on three-body correlations. Two important three-body correlations that arise when we consider a grid point and two atoms, with indices  $j$  and  $k$ , in the neighborhood are detailed below (see Fig. 1).

- i. The three-body correlation that arises due to the overlap between the electronic densities of atoms  $j$  and  $k$  is:

$$\begin{aligned} \rho^{(32)} &= \sum_{j,k} \rho_1(\mathbf{r}, \mathbf{r}_j) \rho_1(\mathbf{r}, \mathbf{r}_k) = \sum_{m,n} c_{mn}^{(32)} \phi_{mn}^{(32)}, \\ \phi_{mn}^{(32)} &= \sum_{j,k} \psi_m(|\mathbf{r} - \mathbf{r}_j|) \psi_n(|\mathbf{r} - \mathbf{r}_k|). \end{aligned} \quad (7)$$

Here,  $c_{mn}^{(32)}$  are the coefficients of this expansion. It is easy to see that  $\rho^{(32)}$  is not sensitive to the distance between atoms  $j$  and  $k$ , i.e. it does not change if atoms  $j$  and  $k$  are located anywhere on the surface of a sphere centered at  $\mathbf{r}$ .

- ii. Next, we consider a correlation that also encodes the proximity between the atoms  $j$  and  $k$ :

$$\begin{aligned} \rho^{(33)} &= \sum_{m,n,o} c_{mno}^{(33)} \phi_{mno}^{(33)}, \quad \text{where} \\ \phi_{mno}^{(33)} &= \sum_{j,k} \psi_m(|\mathbf{r} - \mathbf{r}_j|) \psi_n(|\mathbf{r} - \mathbf{r}_k|) \psi_o(|\mathbf{r}_j - \mathbf{r}_k|). \end{aligned} \quad (8)$$

Schematic illustrations of these correlations are shown in Fig. 1.

### 4. Four-body correlations

To obtain descriptors based on four-body correlations, we consider a grid point and overlaps between the electronic densities of three atoms with indices  $j$ ,  $k$  and  $l$ . These contributions are detailed below:

- iii. The correlation arising due to the overlap between the electronic densities of three atoms  $j$ ,  $k$  and  $l$  at the grid

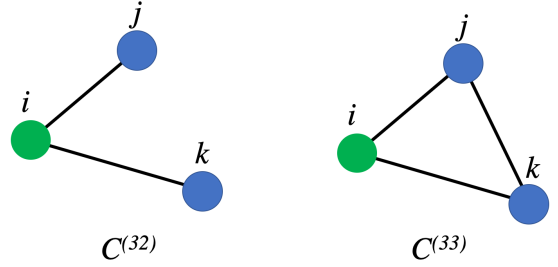


FIG. 1: A schematic representation of correlations due to the overlap between densities of three atoms. Each bond represents an overlap between electronic densities of two atoms. Closed paths or loops represent overlap between densities of all three atoms.

point is captured by (see Fig. 2(b))

$$\begin{aligned} \rho^{(43)} &= \sum_{j,k,l} \rho_1(\mathbf{r}, \mathbf{r}_j) \rho_1(\mathbf{r}, \mathbf{r}_k) \rho_1(\mathbf{r}, \mathbf{r}_l) \\ &= \sum_{m,n,o} c_{mno}^{(43)} \phi_{mno}^{(43)}, \quad \text{where,} \\ \phi_{mno}^{(43)} &= \sum_{j,k,l} \psi_m(|\mathbf{r} - \mathbf{r}_j|) \psi_n(|\mathbf{r} - \mathbf{r}_k|) \psi_o(|\mathbf{r} - \mathbf{r}_l|). \end{aligned} \quad (9)$$

- iv. The correlation that encodes the separation between a pair of neighbors of the grid point is given by

$$\begin{aligned} \rho^{(44)} &= \sum_{m,n,o,p} c_{mnop}^{(44)} \phi_{mnop}^{(44)}, \quad \text{where} \\ \phi_{mnop}^{(44)} &= \sum_{j,k,l} \psi_m(|\mathbf{r} - \mathbf{r}_j|) \psi_n(|\mathbf{r} - \mathbf{r}_k|) \\ &\quad \times \psi_o(|\mathbf{r} - \mathbf{r}_l|) \psi_p(|\mathbf{r}_j - \mathbf{r}_l|) \end{aligned} \quad (10)$$

Geometrically, this correlation accounts for an extra edge between the two neighbors  $j$  and  $l$  of the grid point as shown in Fig. 2(a).

- v. Next, we consider the correlation that arises when two pairs of atoms are connected by edges. For example, in Fig. 2(b), two pairs of neighbors ( $j, l$ ) and ( $k, l$ ) are connected by extra edges and the corresponding four body correlation is given by

$$\begin{aligned} \rho^{(45)} &= \sum_{m,n,o,p,q} c_{mnopq}^{(45)} \phi_{mnopq}^{(45)}, \quad \text{where} \\ \phi_{mnopq}^{(45)} &= \sum_{j,k,l} \psi_m(|\mathbf{r} - \mathbf{r}_j|) \psi_n(|\mathbf{r} - \mathbf{r}_k|) \\ &\quad \times \psi_o(|\mathbf{r} - \mathbf{r}_l|) \psi_p(|\mathbf{r}_j - \mathbf{r}_l|) \psi_q(|\mathbf{r}_k - \mathbf{r}_l|) \end{aligned} \quad (11)$$

- vi. Finally, we consider the correlation that arises when all the three neighbors of a grid point are connected by

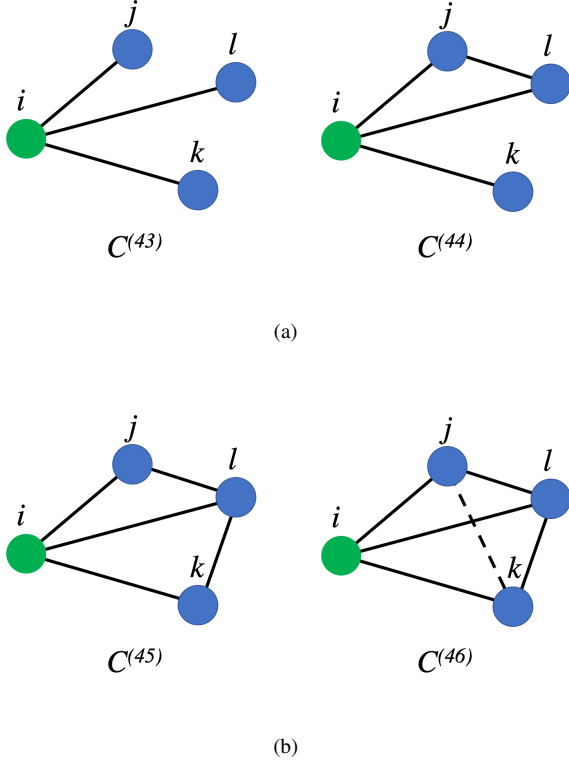


FIG. 2: Correlations due to the overlap between the densities in a cluster containing 4 atoms.

edges.

$$\rho^{(46)} = \sum_{m,n,o,p,q,r} c_{mnopqr}^{(46)} \phi_{mnopqr}^{(46)}, \quad \text{where,}$$

$$\phi_{mnopqr}^{(46)} = \sum_{j,k,l} \psi_m(|\mathbf{r} - \mathbf{r}_j|) \psi_n(|\mathbf{r} - \mathbf{r}_k|) \psi_o(|\mathbf{r} - \mathbf{r}_l|) \\ \times \psi_p(|\mathbf{r}_j - \mathbf{r}_l|) \psi_q(|\mathbf{r}_k - \mathbf{r}_l|) \psi_r(|\mathbf{r}_k - \mathbf{r}_j|)$$
(12)

Intuitively, this procedure can be repeated to generate higher order descriptors. But, as we show in the subsequent sections, our analysis suggests that uncertainties in models containing up to four-body correlations are very low.

### 5. Linear regression model to predict $\rho(\mathbf{r})$

Using these different two, three, four-body correlations we obtain the following model to represent the electronic density at a grid point (with indices  $(i, j, k)$  and spatially located at

$\mathbf{r}_{ijk}$ )

$$\rho(\mathbf{r}_{ijk}) = \sum_n c_n^{(21)} \phi_n^{(21)} + \sum_{m,n} c_{mn}^{(32)} \phi_{mn}^{(32)} + \\ \sum_{m,n,o} \left[ c_{mno}^{(33)} \phi_{mno}^{(33)} + c_{mno}^{(43)} \phi_{mno}^{(43)} \right] + \\ \sum_{m,n,o,p} \left[ c_{mnop}^{(44)} \phi_{mnop}^{(44)} + c_{mnop}^{(54)} \phi_{mnop}^{(54)} \right] + \dots$$
(13)

Let the target electronic density at all the grid points be represented by the vector  $\rho$  and  $\mathbf{c}$  be a vector that contains all the correlation coefficients, i.e.  $\{c_1^{(21)}, c_2^{(21)}, \dots, c_{11}^{(32)}, c_{21}^{(32)}, \dots\}$ . Then, Eq. 13 can be expressed as a linear system of equations as shown below

$$\rho = \mathbb{M}\mathbf{c}. \quad (14)$$

Here,  $\mathbb{M}$  is a matrix, such that the number of rows is equal to the total number of grid points in the training data set, and the number of columns is equal to the total number of correlations present in the many-body expansion in Eq. 13. To obtain the coefficients  $\mathbf{c}$  of this many-body expansion, we use a linear regression framework<sup>29,30</sup> and minimize the following cost function with  $L_2$ -regularization:

$$\Omega_1 = \sum_{S_u} \sum_{i,j,k} \left| \rho_{ijk}(\mathbf{c}) - \rho_{ijk}^{\text{DFT}} \right|^2 + \lambda_1 |\mathbf{c}|_{L_2}^2. \quad (15)$$

Here  $\rho_{ijk}(\mathbf{c}) = \rho(\mathbf{r}_{ijk})$  is the density described in Eq. 13 at grid point  $(i, j, k)$ ,  $\rho_{ijk}^{\text{DFT}}$  is the charge density at the same grid point obtained from a direct DFT calculation. The sum over  $S_u$  is over all the structures and the corresponding charge densities in the training data set. The model in Eq. 15 can be easily modified to incorporate model selection using  $L_1$ -regularization, or a mixture of  $L_1$  and  $L_2$ -regularization.

## B. Total energy prediction

In this section, we present a framework to predict the total energy of a structure. Here we note that the total energy is invariant to global rotation and global translation of the structure and the corresponding ground state charge density. In addition, the total energy,  $E_u = E_u(\rho(\mathbf{r}_u))$ , of a structure (denoted by index  $u$ ) has to be independent of how grid points of the charge density are indexed (i.e. permutation of grid indices). To mitigate these issues, we propose to minimize the following cost function for each structure present in the training data set:

$$\bar{\Omega}_1 = \sum_{i,j,k} \left| \rho_{ijk}(\bar{\mathbf{c}}^{(u)}) - \rho_{ijk}^{\text{DFT}} \right|^2 + \lambda_1 \left| \bar{\mathbf{c}}^{(u)} \right|_{L_2}^2. \quad (16)$$

Thus,  $\Omega$  in Eq. 15 differs from  $\bar{\Omega}_1$  in Eq. 16 because of the additional summation (in Eq. 15) over all structures in the training set. After minimizing  $\bar{\Omega}_1$ , the ground state electronic density  $\rho(\mathbf{r}_u)$  for a structure (denoted by an index  $u$ ) can be

represented by a unique coefficient vector which is denoted by  $\bar{c}^{(u)}$ . Here we note that the linear regression model proposed in Section IIA is to predict the ground state charge density at each grid point based on its local environment. However, to predict  $E_u(\rho(\mathbf{r}_u))$  from  $\rho(\mathbf{r}_u)$ , we seek a set of coefficients  $\bar{c}^{(u)}$  that can uniquely identify the whole structure. Now, to predict the total energy, we use these coefficients as descriptors and train a variety of linear and nonlinear models using different regression techniques.

### 1. Linear regression for total energy prediction

Given a set of correlation coefficients (i.e.  $\bar{c}^{(1)}$ ,  $\bar{c}^{(2)}$ ,  $\bar{c}^{(3)}$ ,  $\dots$  for different structures in the data set), the linear regression model to predict the total energy is given by

$$\Omega_2 = |E(\mathbb{C}) - E_{\text{DFT}}|^2 + \lambda_2 |\boldsymbol{\beta}|_{L_2}^2, \text{ and, } E(\mathbb{C}) = \mathbb{C}\boldsymbol{\beta} \quad (17)$$

Here  $\mathbb{C}$  is a matrix such that the  $u$ -th row of  $\mathbb{C}$  is the coefficient vector  $\bar{c}^{(u)}$  of the  $u$ -th configuration (as described in the previous paragraph) in the training data set, and the number of rows is the number of configurations. The coefficients of this linear model are represented by the vector  $\boldsymbol{\beta}$ .

### 2. Principal Component Regressions for the total energy prediction

To generate a computationally viable model, we seek to minimize the number of structures that are required to train the model in Eq. 17. This means that the number of coefficients or features for each configuration has to be smaller than the number of samples. To solve this problem, we use the principal components analysis (PCA) which is an unsupervised learning method that helps us to build a low dimensional ( $< \dim(\boldsymbol{\beta})$ ) representation of the coefficients  $\bar{c}^{(s)}$ .

The central ideal of PCA is to minimize the error, denoted by  $\epsilon$ , between the original data  $\mathbf{X}$  and its low-dimensional representation (which is denoted by  $\hat{\mathbf{X}}$ ):

$$\epsilon = \|\mathbf{X} - \hat{\mathbf{X}}\|_{\min}. \quad (18)$$

The PCA method uses a linear transformation to project the original data to a subspace of maximum variance and an orthogonality constraint is imposed on this transformation. When the  $\epsilon$  in Eq. 18 is minimized with this orthogonality constraint, we obtain the following covariance matrix,  $\Sigma$

$$\Sigma = \frac{1}{m-1} \mathbf{X}^T \mathbf{X}. \quad (19)$$

Here,  $m$  is the number of observations. Next, we define a matrix  $\mathbf{U}$ , that contains the eigenvectors of the covariance matrix ordered in descending order of the magnitude of their variance – the first column corresponds to the eigenvector of maximum variance and the last column corresponds to the eigenvector with the smallest variance. Next, we select a set of  $k$  eigenvalues (and their corresponding eigenvectors) that account for

most of the total variance (which is usually more than 90%). The eigenvectors corresponding to these  $k$  selected eigenvalues (sorted in the descending order) are stored in the column matrix  $\mathbf{U}(k)$ . The original data is then transformed to a low dimensional representation by using

$$\hat{\mathbf{X}} = \mathbf{X}\mathbf{U}(k). \quad (20)$$

In our case  $\mathbf{X} = \mathbb{C}$ , and we want to obtain a matrix  $\hat{\mathbb{C}}$  with smaller number of features, i.e. the dimensions of the feature space  $\hat{c}$  for each configuration is smaller than  $\bar{c}$ . Next, Eq. 17 is solved using  $\hat{\mathbb{C}}$  instead of  $\mathbb{C}$ .

To evaluate the number of principal components necessary to get a good model, we analyze the convergence of the coefficient of determination,  $R^2$ , and the root mean square error, RMSE, with respect to the number of principal components. A good fit corresponds to the case when  $R^2 \rightarrow 1$ , i.e. the mean squared error is much smaller than the variance of the data.

### 3. Nonlinear regressions of the total energy

To capture existing nonlinearities in the representation of the total energy using the features  $\hat{c}$  (or  $\bar{c}$ ), we use non-parametric regressions, such as kernel ridge and Gaussian process regressions.<sup>29–31</sup> The kernel ridge regression incorporates nonlinearity into the model by using a nonlinear function also called the kernel (denoted by  $k(\bar{c}_i, \bar{c}_j)$  for two different structures  $i$  and  $j$ ) that captures the similarity between two structures. The total energy of a test structure with features  $\mathbf{c}^*$  is then given by

$$E^* = \sum_i \alpha_i \cdot k(\bar{c}_i, \bar{c}^*) \quad (21)$$

and the coefficients  $\alpha$  are obtained by minimizing the cost function in Eq. 17. The kernel function is positive definite and it shapes the way the features are compared in high dimensional space; the explicit equations to find the coefficients of the kernel regressions can be found elsewhere.<sup>30–32</sup>

Gaussian process regression is a nonlinear regression technique that is very similar to kernel ridge regression; the difference arises from the assumption that the coefficients  $\alpha_i$  in Eq. 21 are normally distributed in case of the Gaussian process regression. As a consequence, the regression output is also normally distributed.<sup>32</sup> The covariance of the output distribution and its error is defined by the corresponding kernel,  $\mathbf{K}$  which is given by

$$\mathbf{K} = \bar{\mathbf{K}} + \sigma^2 \mathbf{I}. \quad (22)$$

Here  $\bar{\mathbf{K}}_{ij} = k(\bar{c}_i, \bar{c}_j)$  and  $\sigma$  defines the strength of the noise, and its role is similar to the regularization coefficient used in linear regression. To model the total energies using the Gaussian process regression, we use the radial basis function ker-

nel, i.e.

$$K_{ij} = \lambda^2 \exp\left(-\gamma^2 |\mathbf{c}_i - \mathbf{c}_j|^2\right) + \sigma^2 \delta_{ij}. \quad (23)$$

This kernel has been successfully used for a wide range of problems.<sup>32</sup> In Eq. 23, the parameter  $\gamma$  scales the difference between the feature vectors,  $\lambda$  scales the exponential term, and  $\sigma$  is the amplitude of the noise and controls the strength of the regularization.

The kernel and Gaussian process regression methods differ in the way the hyper-parameters of the models are optimized. In the case of kernel ridge regression, the commonly used model selection methods are the leave-out-one, three way hold-out, or  $k$ -fold cross-validation. In Gaussian process regression, the hyper-parameters are typically calculated by either maximizing the log-likelihood function, by using cross-validation along with the log-likelihood method, or by using the Markov chain Monte Carlo method. For the analysis presented here we use the three-way hold-out method for cross-validation, and log-likelihood maximization to obtain the model hyper-parameters for kernel ridge regression and Gaussian process regression, respectively.

### III. RESULTS: GROUND STATE CHARGE DENSITY

#### A. DFT data for testing

To train and test our model for the ground state charge density and total energy predictions we use amorphous Ge as the model system. This choice is motivated by the fact that many machine learning techniques for interatomic potential generation fail to appropriately capture the interactions between atoms in a liquid or in disordered systems. For training and testing purposes, we generated two data sets:

- a) *Data set A*: To obtain the first data set, we start with a disordered Ge supercell containing 512 atoms with edge lengths of  $23.5 \times 23.5 \times 23.5 \text{ \AA}^3$ . This structure is obtained by melting a crystalline solid and quenching the system to 100 K. From this reference structure, we generate 500 configurations by perturbing the atomic positions in the disordered Ge supercell by using random numbers uniformly distributed in the interval  $(-\delta, \delta) \text{ \AA}$ , where  $\delta$  is set to 2% of the supercell edge length.
- b) *Data set B*: Next, we generate a second reference structure by perturbing (perturbation amplitude is 1% of the edge length) the atomic positions of a disordered Ge structure. Using this reference structure as the seed, we generate another set of 500 perturbed structures by using random numbers uniformly distributed in the interval of  $(-1, 1) \text{ \AA}$ .

All density functional theory calculations are performed using the plane wave basis density functional theory (DFT) implementation in Vienna Ab-initio Simulation Package

(VASP)<sup>33,34</sup> using the PBE<sup>35</sup> exchange correlation functional. We use a plane wave cut-off of 560 eV to expand the wavefunctions and a  $2 \times 2 \times 2$   $k$ -point mesh to perform the Brillouin zone integrations. We use supercells containing 512 Ge atoms and the supercell edge lengths are equal to 23.5  $\text{\AA}$ .

#### B. Predicting the charge density

To train a model that can accurately reproduce the ground state charge density at each grid point, correlation functions described in Section II are evaluated using a set of Chebyshev polynomials of first kind. Chebyshev polynomials satisfy the following orthogonality relation ( $m, n > 0$ )

$$\int_{-1}^1 \psi_n(s) \psi_m(s) \frac{ds}{\sqrt{1-s^2}} = \frac{\pi}{2} \delta_{mn} \quad (24)$$

To evaluate a Chebyshev polynomial, the input argument has to be in the range of  $[-1, 1]$ . Thus, the distance,  $r$ , between an atom and a grid point is scaled according to the following prescription

$$s = \cos \left[ \frac{r - r_{\min}}{r_{\max} - r_{\min}} \right]. \quad (25)$$

Here,  $r_{\max}$  and  $r_{\min}$  are parameters that correspond to the maximum and minimum distances between an atom and a grid point. For computational efficiency purposes while evaluating the neighborhood of a grid point, we introduce a cutoff radius. Thus,  $r_{\max}$  is set to be equal the cutoff radius.

Next, we calculate the number of basis functions needed to model the two-body correlations. For this, we use 20-40 structures (equal number of structures from each of the two sets in Section IIIA) and corresponding ground state charge densities to train the model and another 20 structures (10 each from the sets A and B in Section IIIA) for testing. The charge density obtained from DFT calculations is represented using a  $280 \times 280 \times 280$  (supercell dimensions are  $23.50 \times 23.50 \times 23.50 \text{ \AA}^3$ ) grid size. To reduce data redundancy, we use charge density information from grid points separated by 10, 14, 20 or 28 grid points along each axes (i.e. along each dimension we use  $280/10 = 28$ ,  $280/14 = 20$ ,  $280/20 = 14$  and  $280/28 = 10$  grid points to train our model, respectively).

For two-body correlations, Fig 3(a) shows the RMSE in predicted values of the electronic density at  $28^3 \times 20$  grid points (i.e.  $28^3$  grid points each from 20 charge density files) from the test data set. To calculate the number of Chebyshev polynomials needed to capture the two-body correlations, we truncate the model in Eq. 13 to the following

$$\rho(\mathbf{r}_{ijk}) = \sum_{n=0}^{N_{21}} c_n^{(21)} \left[ \sum_{p=1}^{M_{ijk}} \psi_n(|\mathbf{r}_{ijk} - \mathbf{r}_p|) \right] = \sum_{n=0}^{N_{21}} c_n^{(21)} \phi_n^{(21)} \quad (26)$$

where,  $M_{ijk}$  is the number of neighbors of grid point  $(i, j, k)$  and  $N_{21}$  is the number of Chebyshev polynomials used to rep-

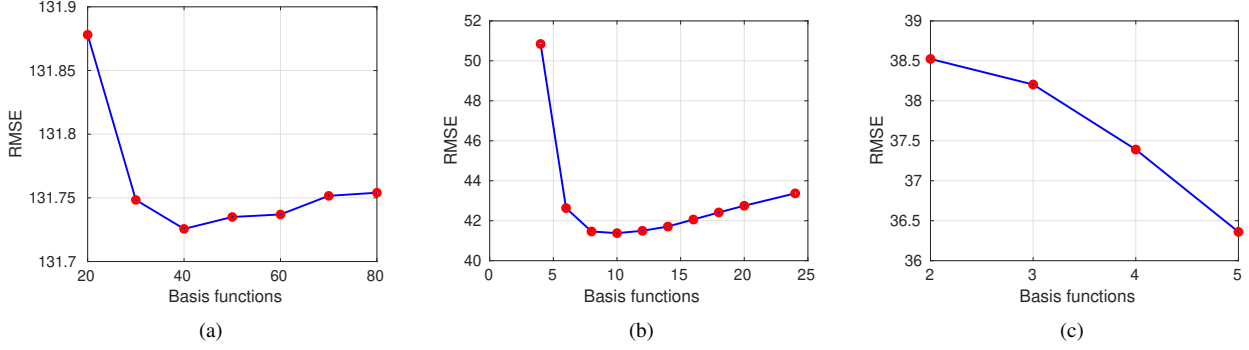


FIG. 3: The optimum number of basis functions required to describe a correlation corresponds to the minimum value in the RMSE profile. Shown here are the variations in the RMSE scores with respect to the number of basis functions used to capture 3(a) two-body, 3(b) correlations with three bonds, and 3(c) correlations with four bonds. Note that the charge density values have not been scaled by the inverse of the supercell volume (i.e. by  $23.5^3 \text{ \AA}^3$ ). Thus, the minima in these plots correspond to a RMSE of 0.01 (a),  $3.19 \times 10^{-3}$  (b) and  $2.80 \times 10^{-3}$  (c)  $e/\text{\AA}^3$  in the predicted charge densities.

represent the two-body correlations. The RMSE error in Fig 3(a) shows a marginal decrease as the number of basis functions increases and reaches a minimum at 40 Chebyshev polynomials. Thus, we use 40 basis functions to capture two-body correlations in the subsequent analysis. Using a similar procedure, we see that the RMSE reaches a minimum when Chebyshev polynomials of order 20 per bond are used to represent three-body correlations with two bonds (see Fig. 1, left). This means that there are  $21 \times (21 + 1) / 2 = 231$  correlation coefficients for this type of three-body correlation.

Figure 4 shows the convergence of the RMSE, for a model containing correlations with one- and two-bonds, respect to a few parameters of the model. For example, in Fig. 4(a) we see that the RMSE score decreases with an increase in the number of grid points per charge density file: The RMSE decreases from 74.39 ( $5.72 \times 10^{-3} e/\text{\AA}^3$ ) to 68.90 (i.e.  $5.30 \times 10^{-3} e/\text{\AA}^3$ ) when the number of grid points increases from 10 grid points/axis (i.e. 1000 grid points per charge density file) to 28 grid points/axis. Similarly, Fig. 4(b) shows the convergence of the RMSE with respect to the cut-off radius. Thus, for the results shown in Fig. 3 we use  $6.50 \text{ \AA}$  as the cut-off radius and this results in a RMSE of  $5.4 \times 10^{-3} e/\text{\AA}^3$  (see Fig. 4(b)).

Figure 3(b) shows the number of basis functions per bond needed to capture correlations with three-bonds, i.e.  $c^{(33)}$  and  $c^{(43)}$ . Since both of these correlations contain three-bonds, we assign the same number of Chebyshev polynomials to both of them. Thus, for this analysis, the model in Eq. 13 is reduced to the following form

$$\rho(\mathbf{r}_{ijk}) = \sum_{n=0}^{40} c_n^{(21)} \phi_n^{(21)} + \sum_{n=0}^{20} \sum_{m=n}^{20} c_{mn}^{(32)} \phi_{mn}^{(32)} + \sum_{n=0}^{N_{33}} \sum_{m=n}^{N_{33}} \sum_{o=m}^{N_{33}} \left[ c_{mno}^{(33)} \phi_{mno}^{(33)} + c_{mno}^{(43)} \phi_{mno}^{(43)} \right]. \quad (27)$$

From Fig. 3(b) we see that the RMSE score reaches a minimum value when basis functions (per bond) of index 11 are used. Thus, for all subsequent calculations, we use

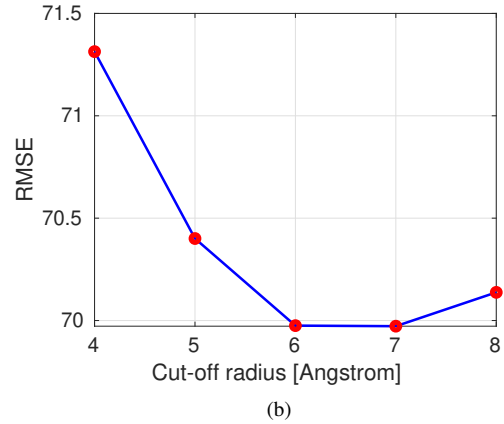
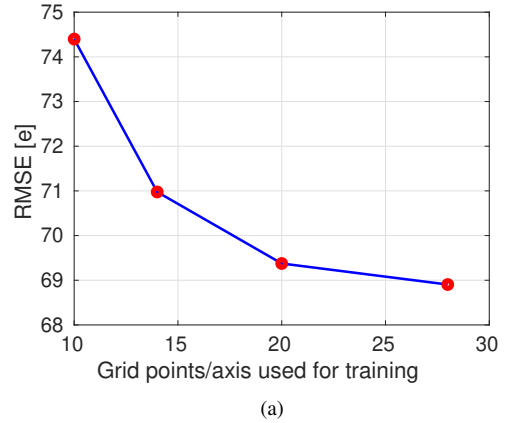


FIG. 4: Shown here is the convergence of the RMSE with respect to the number of grid points along each edge vector and cut-off radius used to determine the number of neighbors surrounding an atom. Note that the charge density values are scaled by the inverse of the supercell volume (i.e. by  $23.5^3 \text{ \AA}^3$ ). Thus, the minima in (a) and (b) correspond to RMSE of  $\sim 5.4 \times 10^{-3} e/\text{\AA}^3$

$2 \times (11 \times 12 \times 13/6) = 572$  correlation coefficients for both  $c_{mno}^{(33)}$  and  $c_{mno}^{(43)}$  correlations. This means that a model that contains correlations with one, two, and three bonds has in total  $(40 + 231 + 572) = 843$  correlation components and an equal number of correlation coefficients. Figure 3(c) shows that the RMSE score decreases from a minimum value of  $3.19 \times 10^{-3} \text{ e}/\text{\AA}^3$  in Fig. 3(b) to  $2.92 \times 10^{-3} \text{ e}/\text{\AA}^3$  when correlations with four bonds are present in the model. For this analysis, we use a model containing four- and five-body correlations with four bonds:

$$\begin{aligned} \rho(\mathbf{r}_{ijk}) = & \sum_{n=0}^{40} c_n^{(21)} \phi_n^{(21)} + \sum_{n=0}^{20} \sum_{m=n}^{20} c_{mn}^{(32)} \phi_{mn}^{(32)} + \\ & \sum_{n=0}^{10} \sum_{m=n}^{10} \sum_{o=m}^{10} \left[ c_{mno}^{(33)} \phi_{mno}^{(33)} + c_{mno}^{(43)} \phi_{mno}^{(43)} \right] + \\ & \sum_{n=0}^{N_{44}} \sum_{m=n}^{N_{44}} \sum_{o=m}^{N_{44}} \sum_{p=o}^{N_{44}} \left[ c_{mnop}^{(44)} \phi_{mnop}^{(44)} + c_{mnop}^{(54)} \phi_{mnop}^{(54)} \right]. \end{aligned} \quad (28)$$

The RMSE score decreases as more Chebyshev polynomials are included in the model (see Fig. 3(c)), but the computation cost for evaluating these correlation components increases very quickly. For example, when Chebyshev polynomials of index  $n$  are included, the number of correlation components is given by  $(n+1)(n+2)(n+2)(n+3)/12$ . Thus, we use only a few basis functions to capture correlations with four bonds.

Figure 5(a) shows the systematic increase in the accuracy of predictions as the number of bonds in the correlation increases. These results suggest that a model that includes correlations with one, two and three bonds can very accurately capture the local environment around a grid point and hence can to predict the ground state electronic charge density.

Figure 5(b) compares errors from models containing different many-body terms. For example, predictions made, at different grid points, by using only two-body correlations (red markers) results in systematic errors at small as well as large values of the charge density. On the other hand, predictions made (at different grid points) by using models containing correlations with two and three bonds (blue markers) do not exhibit systematic errors and predictions made by using models containing correlations with four bonds (black markers) have significantly higher accuracy.

#### IV. RESULTS: TOTAL ENERGY

Next, to predict the total energy of an atomic configuration, we use the coefficients of the many-body expansion (of the electronic density) as descriptors, or features, to fit the total energy by using the parametric and the non-parametric regression methods described in Section II. Thus, Eq. 16 is solved for each structure in the data set and a coefficient vector (i.e.  $\bar{c}_u$ ) is obtained for each structure (with index  $s$ ).

We conjecture that these coefficients are good descriptors since they describe the amplitudes of each many-body contri-

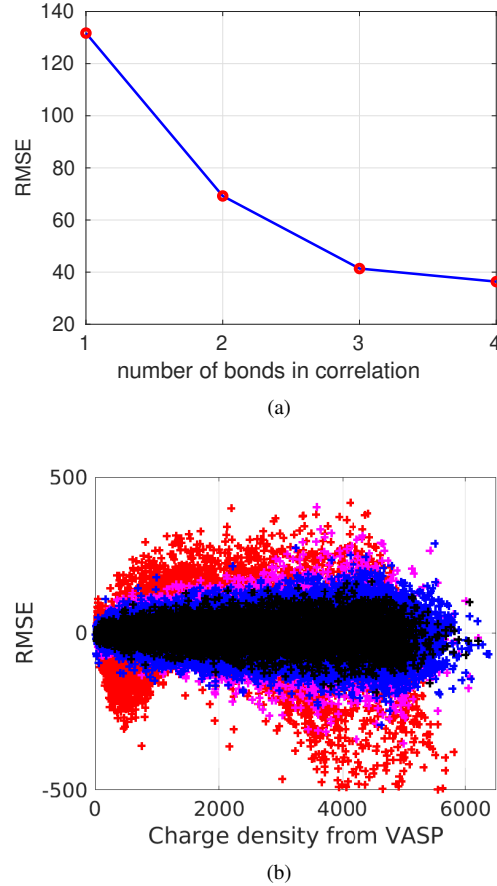


FIG. 5: 5(a) shows the monotonous decrease in the RMSE with the increase in the order of correlations present in the model. 5(b) shows that predictions made using only two-body correlations (red markers) results in systematic errors in the predicted charge density. On the other hand, predictions made by using models containing correlations with two and three bonds (blue markers) do not exhibit systematic errors. Predictions made by using models containing correlations with four bonds significantly increases the accuracy. Note that the charge density values are not scaled by the inverse of the supercell volume (i.e. by  $23.5^3 \text{ \AA}^3$ ).

bution to the electronic density. However, the number of coefficients also depends on the number of Chebyshev functions necessary to capture high-frequency density variations. We use 40 Chebyshev basis functions to describe the two-body correlations, Chebyshev polynomials of index 20/bond to describe the correlations with two bonds and Chebyshev polynomials of index 11/bond to describe the correlations with three-bonds. This is based on the convergence analysis presented in Section IIIB. Thus, the number of coefficients, or features, of the data set is 843. In the subsequent sections, we present an analysis of the total energies predicted using various linear and nonlinear regression techniques.

To generate the model, we obtain training and validation

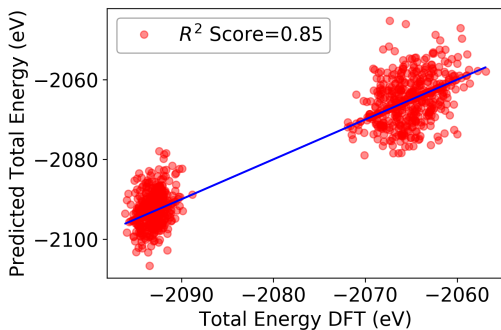


FIG. 6: Predicted total energies of structures in the validation set using features in the whole feature space. The two clusters correspond to structures in sets A and B (see Section III A).

sets by selecting an equal number of structures from the two sets mentioned in Section III A, i.e. we use 200 samples for training, another 200 samples for validation and the remaining unseen samples are used to quantify the predictive capabilities of the models. Validation is done using the three-way hold-out method and the regularization coefficient is obtained by minimizing the error using the Nelder-Mead algorithm.

#### A. Linear Ridge Regression Model

To model the total energy of a configuration using Eq. 17, we use descriptors (i.e. coefficient vectors  $\bar{c}^{(s)}$ ) in the full feature space and optimize the  $R^2$  score to obtain the optimum value of the regularization coefficient  $\lambda$  in Eq. 17. The total energies of structures in the validation data set obtained from this  $\beta$  is shown in 6. The solid line in Fig. 6 corresponds to a scenario where the predictions made from a model agrees perfectly with the DFT-calculated total energies. As explained in Section III A, there are two clusters in our data set and they correspond to different magnitudes of perturbation of atomic positions. In Fig. 6, total energies predicted for structures in data set A (i.e. the lower-left cluster) show a smaller variance compared to the predictions made for the structures in data set B (i.e. the upper-right cluster).

It is clear that these results correspond to an over-fitted regime: The variance in the predicted energies for the input data set is smaller than the variance in the predicted energies for the unseen data. In principal, to reach a better bias-variance trade off, the model needs more data to learn the features properly. This issue can be tackled by simply increasing the amount of training samples. However, our goal here is to minimize the overall variance as well as the number of training samples. Thus, an alternative approach to achieve this goal is to reduce the model complexity by feature selection or dimensionality reduction. For this purpose, we use the principal component analysis (PCA) method to reduce the dimension of the features space and reach a better model performance in which 200 samples are used for training, another 200 samples are used for validation, and the remaining unseen data are used for testing.

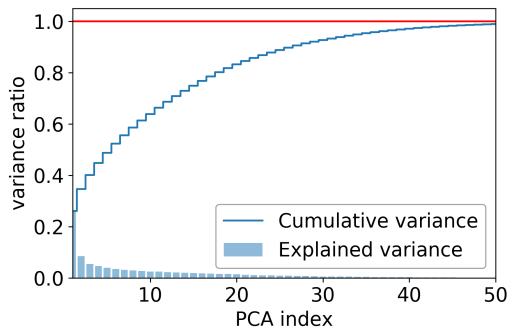


FIG. 7: The contributions of the different principal components to the total variance is shown using the solid line. The solid bars denote the magnitude of the normalized eigenvalue of along each principal components.

#### B. Dimensionality reduction using principal component analysis

To reduce the dimensionality of the feature space, we use PCA on the set of coefficient vectors  $\{\bar{c}^{(1)}, \bar{c}^{(2)}, \dots\}$  (solutions of the linear system in Eq. 16 for different structures and the corresponding charge densities in the training data set). Figure 7 shows the magnitude of the normalized eigenvalues arranged in descending order. These normalized eigenvalues can be interpreted as the magnitude of the variance of the corresponding eigenvector, i.e. the largest eigenvalue encodes more variance as explained in the methods section.

Figure 7 also displays the cumulative variance - interestingly, using only 20 principal components our model can capture 80% of the total variance in the data. In addition, as we systematically increase the number of principal components, the cumulative sum quickly approaches 1 with only 50 normalized eigenvalues which is just 6% of the size of the feature space. Thus, PCA helps us to select only a few relevant features, thereby reducing model complexity (the number of principal components  $\ll \dim(\bar{c})$ , i.e. the size of the feature space). In addition, PCA avoids collinearity among the features by using principal components that are, by design, orthogonal to each other.

After projecting the coefficient vectors, i.e. the descriptors, into the important principal components, we use linear and nonlinear regression techniques to train our model. This decrease in dimension of the feature space (due to PCA) allows us to use a smaller data set for training these models resulting in a better bias-variance trade off.

#### C. Principal components regression

Next, we use linear ridge regression on the PCA-projected data. For this, we need to identify the minimum number of principal components required to converge the  $R^2$  score of the model. Figure 8 illustrates the convergence of the  $R^2$  score with respect to the number of principal components. It is clear that by using only ten principal components we can capture 90

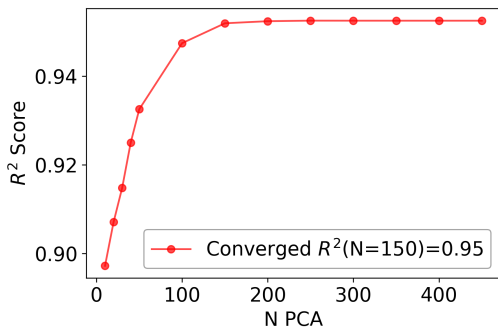


FIG. 8: Shown here is the convergence of the  $R^2$  scores of the predicted total energies using a ridge regression model as a function of the number of principal components.

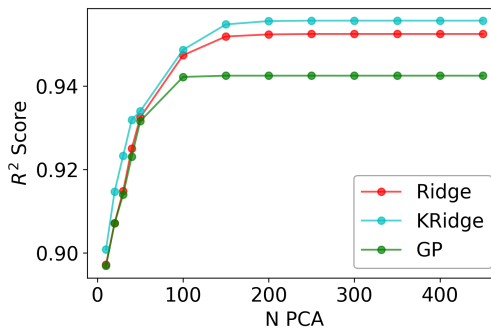


FIG. 10: Shown here is the convergence of the  $R^2$  scores (for the three different nonlinear regression techniques) with respect to the number of principal components used.

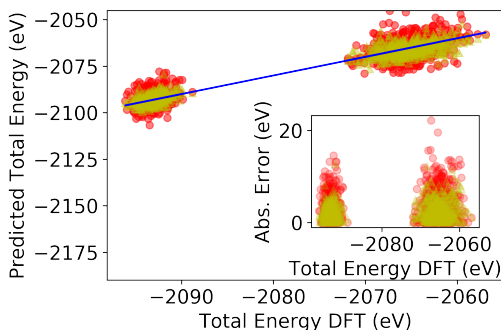


FIG. 9: Shown here is a comparison between the DFT calculated total energies and the total energies predicted using two ridge regression models: one that uses descriptors in the whole feature space (red circles), and another that uses descriptors projected on 150 principal components (triangles). The solid line (blue) corresponds to perfect agreement with the DFT data.

% of the variation. Nonetheless, by increasing the number of principal components to 150, we obtain a model that covers 96% of the variation.

Figure 9 compares the predictions made by using two different linear regression models. The first model uses descriptor vectors in entire feature space while the second model uses descriptor vectors projected into a space of 150 principal components. The advantage of using principal component regression is evident from the fact that by using only 150 principal components and total energies of 200 training structures we are able to significantly improve the performance of the model. In addition, the fact that by using only 150 principal components our model achieves a  $R^2$  score of 96% illustrates that deviations in the predicted values have diminished significantly. Thus, principal component regression is able to capture important features of the model.

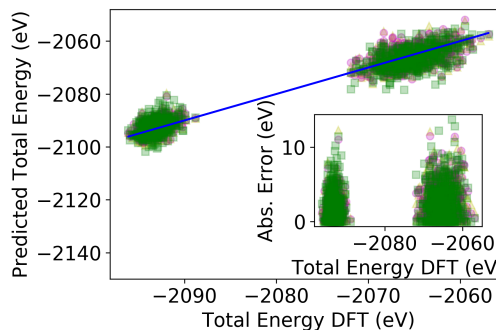


FIG. 11: A comparison of the DFT calculated and predicted total energies for models obtained by using linear (triangles), Gaussian process (squares), and kernel ridge (circles) regression techniques. The solid line (blue) corresponds to perfect agreement with the DFT data.

#### D. Nonlinear models

Next, we explore the nonlinear characteristics of the descriptors using kernel-based methods like kernel ridge regression and Gaussian process regression. To this end, we use a Gaussian kernel and descriptors projected into the space of a few selected principal components.

Figure 10 displays the convergence of the  $R^2$  score of these kernel methods and compares them to predictions made using the principal component regression method presented in the previous section. It is easy to see that the linear and kernel ridge regression models exhibit similar convergence behavior and their respective  $R^2$  scores converges when  $\sim 150$  principal components are present in the models. In addition, the difference in their converged  $R^2$  scores (in Fig. 10) is less than 1%, meaning that these two models capture similar information from the training data. From Fig. 10, we see that even though the  $R^2$  score of the Gaussian process regression model is similar to the kernel and linear ridge regression models, it converges to a value that is about 3% less than these two models.

Figure 11 compares the total energies predicted using both

	Ridge	KRidge	GP
$R^2$	0.9784	0.9784	0.9753
RMS (eV)	2.909	2.7876	3.1084
MAE(eV)	2.1531	2.0176	2.1648

TABLE I: Performance of the linear and nonlinear regression models for all structures in the data set.

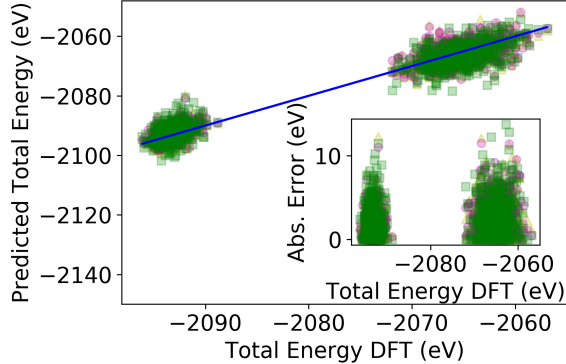


FIG. 12: Shown here is the distribution of the absolute errors in the predicted total energies for all structures in the data set using ridge, kernel and GP regression techniques.

linear and nonlinear regression models. Finally, we analyze the performance of our models using several statistical measures, i.e. the  $R^2$  score, the mean squared error (MSE) and the mean absolute error (MAE) for all the structures in the two data sets described in Section IIIA. These values are listed in Table I.

Figure 12 shows that the histograms of the absolute errors in the predicted total energies for each configuration (in the whole data set) using three different models exhibit similar trends. Thus, from a statistical point of view, these three models offer equivalent performance. Table II also compares the performance of the models using different metrics: mean error, maximum positive and negative errors per supercell and per atom. Thus, the maximum absolute errors are 12.31, 11.50 and 13.71 eV/supercell for ridge, kernel ridge and Gaussian process regressions, respectively meaning that the maximum absolute error per atom is 0.027 eV which is less than the chemical accuracy (1 kcal/mol = 0.043 eV/atom).

## V. SUMMARY AND DISCUSSIONS

Our results show that descriptors based on many-body correlations can effectively capture local neighborhood information. For our analysis, these many-body descriptors are calculated using a set of Chebyshev polynomials (and their products), but any other set of orthogonal polynomials can also be used. Using these descriptors we are able to reproduce ground state electronic charge densities of amorphous structures to a high level of accuracy. It is possible to systematically im-

Measure/Method	Ridge	KRR	GPR
maximum negative error/supercell	-8.09	-9.26	-10.24
maximum positive error/supercell	9.82	9.20	12.31
mean error/atom	0.03	0.02	0.03
maximum negative error/atom	-0.017	-0.018	-0.020
maximum positive error/atom	0.019	0.018	0.024

TABLE II: A comparison of the performance of models obtained by using three nonlinear regression methods using different metrics.

prove the accuracy by incorporating higher order many-body correlations. In addition, we are able to generate reliable models using only a few tens of structures and their ground state charge densities. This is much smaller than the hundreds of structures required to train some of the other models presented in the literature.

Many other descriptors have been proposed in the literature: for example, Brockherde et al. used cosine functions to represent the ground state charge density, while Grisafi et al. used atom-centered symmetry-adapted basis function based on spherical harmonics.<sup>4,5</sup> However, from the cross-validation based testing approach presented in Section III B, it seems that the accuracy of a model containing a particular type of correlation cannot be systematically improved by simply increasing the number of orthogonal basis functions. This is because, beyond a certain value of the RMSE score, increasing the number of basis functions can lead to over-fitting. On the other hand, by incorporating two-, three- and four-body correlations, we are able to systematically improve the predictive capability of our models.

The role played by different many-body correlations may not be easily evident in some of the popularly used descriptors in the literature. For example, the bi-spectrum basis functions used in Ref. [4] can capture up to four body correlations (with three bonds), but these correlations correspond to  $c^{(32)}$  (shown in Fig. 1(left)) and  $c^{(43)}$  (shown in Fig. 2 (first column, left)) and do not include correlations with closed loops (such as  $c^{(33)}$ ). We see that correlations with closed loops, like  $c^{(33)}$ ,  $c^{(44)}$ , ...,  $c^{(46)}$ , are more effective than correlations without closed loops in enhancing the model performance. Here, we note that the importance of systematically incorporating many-body correlations can also be understood from the fact that simple metals (like Cu, Ag, Al, Au) have been successfully modeled using embedded-atom-method type of interatomic potentials (containing only two-body interactions and their products), but three-body interactions are needed to model elements like Si and Ge.

Amplitudes of these many-body correlations are used to model the total energy from the ground state charge density within chemical accuracy. These amplitudes are invariant to

global rotation/translation and permutation of charge density grid indices and hence are useful to uniquely capture the distribution of electronic density corresponding to a distribution of atoms. In the future, we plan to further explore model reduction using compressed sensing to decrease the number of training samples required to optimize the linear system in Eq. 17.

Brockherde et al.<sup>2</sup> were able to reproduce total energies of small molecules, like H<sub>2</sub> and H<sub>2</sub>O, with high accuracy (mean average error  $\sim 0.01$  kcal/mol) using only 10 and 20 structures, respectively. But, for systems, like benzene and ethane (that contain more atoms than that present in H<sub>2</sub> and H<sub>2</sub>O), the number of structures required to achieve a mean average error of 0.37 kcal/mol increased by two orders of magnitude. Perhaps this is an indication that the local electronic density around an atom can be used accurately map the energy of the atom, and the sum of these energies can be used to accurately calculate the total energy of the system. But, descriptors based on the total electronic density of the system (containing as much as 512 atoms in our case) can perhaps capture many important global characteristic features of the system, but fail to capture salient details of  $\rho(\mathbf{r})$  close to bond centers. Thus, in future, we plan to explore a framework to model the total energy as sum of energies of individual atoms and these atomic

energies can be obtained from the charge density in the vicinity of the atom.

### Acknowledgments

The authors wish to thank John Klepeis, Lorin Benedict, Arthur Tamm, ShinYoung Kang, Seung Ho Hahn and Chirraag Nataraj for numerous stimulating discussions. A. S. wishes to thank Mark Tuckerman for valuable suggestions and encouragement to work on this problem during his visit to LLNL. This work was performed under the auspices of the U.S. Department of Energy by Lawrence Livermore National Laboratory under Contract DE-AC52-07NA27344. Computing support for this work came from the Lawrence Livermore National Laboratory (LLNL) Institutional Computing Grand Challenge program.

### Data availability

The data that support the findings of this study are available from the corresponding author upon reasonable request.

\* Electronic address: samanta1@llnl.gov

- <sup>1</sup> K. Mills, M. Spanner, and I. Tamblin, *Physical Review A* **96**, 042113 (2017).
- <sup>2</sup> F. Brockherde, L. Vogt, L. Li, M. E. Tuckerman, K. Burke, and K.-R. Müller, *Nature Communications* **8**, 872 (2017).
- <sup>3</sup> H. Ji and Y. Jung, *Journal of Chemical Physics* **148**, 241742 (2018).
- <sup>4</sup> A. Grisafi, A. Fabrizio, B. Meyer, D. M. Wilkins, C. Corminboeuf, and M. Ceriotti, *ACS Central Science* **5**, 57 (2019).
- <sup>5</sup> A. Grisafi, D. M. Wilkins, G. Csányi, and M. Ceriotti, *Physical Review Letters* **120**, 036002 (2018).
- <sup>6</sup> A. Fabrizio, A. Grisafi, B. Meyer, M. Ceriotti, and C. Corminboeuf, *Chem. Sci.* **10**, 9424 (2019).
- <sup>7</sup> R. Nagai, R. Akashi, and O. Sugino, arXiv:1903.00238 (2019).
- <sup>8</sup> A. Chandrasekaran, D. Kamal, R. Batra, C. Kim, L. Chen, and R. Ramprasad, *npj Computational Materials* **5**, 22 (2019).
- <sup>9</sup> B. Kolb, L. C. Lentz, and A. M. Kolpak, *Scientific Reports* **7**, 1192 (2017).
- <sup>10</sup> A. V. Sinititskiy and V. S. Pande, arXiv:1809.02723 (2018).
- <sup>11</sup> S. Dick and M. Fernandez-Serra, *Journal of Chemical Physics* **151**, 144102 (2019).
- <sup>12</sup> E. Schmidt, A. T. Fowler, J. A. Elliott, and P. D. Bristowe, *Computational Materials Science* **149**, 250 (2018).
- <sup>13</sup> G. Ferré, J.-B. Mailliet, and G. Stoltz, *Journal of Chemical Physics* **143**, 104114 (2015).
- <sup>14</sup> R. Drautz, *Physical Review B* **99**, 014104 (2019).
- <sup>15</sup> A. Samanta, *Journal of Chemical Physics* **149**, 244102 (2018).
- <sup>16</sup> L. Zhang, J. Han, H. Wang, R. Car, and W. E, *Physical Review Letters* **120**, 143001 (2018).
- <sup>17</sup> L. Zhang, D.-Y. Lin, H. Wang, R. Car, and W. E, *Physical Review Materials* **3**, 023804 (2019).
- <sup>18</sup> A. P. Bartók, R. Kondor, and G. Csányi, *Physical Review B* **87**, 184115 (2013).
- <sup>19</sup> A. Glielmo, P. Sollich, and A. De Vita, *Physical Review B* **95**, 214302 (2017).
- <sup>20</sup> M. Rupp, A. Tkatchenko, K.-R. Müller, and O. A. von Lilienfeld, *Physical Review Letters* **108**, 058301 (2012).
- <sup>21</sup> R. K. Lindsey, L. E. Fried, and N. Goldman, *Journal of Chemical Theory and Computation* **13**, 6222 (2017).
- <sup>22</sup> L. Koziol, L. E. Fried, and N. Goldman, *Journal of Chemical Theory and Computation* **13**, 135 (2017).
- <sup>23</sup> A. Takahashi, A. Seko, and I. Tanaka, *Physical Review Materials* **1**, 063801 (2017).
- <sup>24</sup> A. P. Bartók, M. C. Payne, R. Kondor, and G. Csányi, *Physical Review Letters* **104**, 136403 (2010).
- <sup>25</sup> V. Botu and R. Ramprasad, *International Journal of Quantum Chemistry* **115**, 1074 (2015).
- <sup>26</sup> A. Seko, A. Takahashi, and I. Tanaka, *Physical Review B* **90**, 024101 (2014).
- <sup>27</sup> A. V. Shapeev, *Multiscale Modeling and Simulation* **14**, 1153 (2016).
- <sup>28</sup> M. Gastegger, L. Schwiedrzik, M. Bittermann, F. Berzsényi, and P. Marquetand, *Journal of Chemical Physics* **148**, 241709 (2018).
- <sup>29</sup> T. Hastie, R. Tibshirani, and J. Friedman, *The Elements of Statistical Learning: Data Mining, Inference, and Prediction* (2016).
- <sup>30</sup> C. M. Bishop, *Pattern Recognition and Machine Learning* (2016).
- <sup>31</sup> M. Rupp, *International Journal of Quantum Chemistry* **115**, 1058 (2015).
- <sup>32</sup> D. J. C. MacKay, *Information Theory, Inference and Learning Algorithms* (2002).
- <sup>33</sup> G. Kresse and J. Furthmüller, *Physical Review B* **54**, 11169 (1996).
- <sup>34</sup> G. Kresse and J. Furthmüller, *Computational Materials Science* **6**, 15 (1996).
- <sup>35</sup> J. P. Perdew, K. Burke, and M. Ernzerhof, *Physical Review Letters* **77**, 3865 (1996).